Nano Energy 107 (2023) 108182

Contents lists available at ScienceDirect

Nano Energy

journal homepage: www.elsevier.com/locate/nanoen

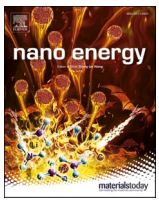

High performance additional mass enhanced film structure triboelectric nanogenerator for scavenging vibration energy in broadband frequency range

Hongyong Yu [a,1], Ziyue Xi [a,1], Yiping Zhang [a], Ruijiang Xu [a], Cong Zhao [a], Yawei Wang [a], Xinyang Guo [a], Yue Huang [a], Jianchun Mi [a,b], Yejin Lin [a], Taili Du [a,*], Minyi Xu [a,*]

[a] Dalian Key Lab of Marine Micro/Nano Energy and Self-powered System, Marine Engineering College, Dalian Maritime University, Dalian 116026, China
[b] College of Engineering, Peking University, Beijing 100871, China

ARTICLE INFO

Keywords:
Triboelectric nanogenerator
Vibrational energy scavenging
Additional mass
Broadband frequency range

ABSTRACT

It is highly desired to develop high performance vibration energy scavengers to power amounted and distributed sensors along with the era of Internet of Things. This study proposes a novel additional mass enhanced film structure triboelectric nanogenerator (AMF-TENG) for efficiently scavenging broadband vibration energy. The AMF-TENG is composed of an additional mass, a fluorinated ethylene propylene (FEP) film with a carbon electrode, and a conductive fabric fixed on a hollow frame. The additional mass can enhance the electrical output of the AMF-TENG by 25.5 times due to the vibration amplitude and contact forces between the FEP film and conductive fabric are greatly amplified. The utilization of a hollow frame makes the electrical output of AMF-TENG 150% higher than the enclosed frame. Theoretical analysis and experimental studies were carried out to investigate the design parameters. The experimental results indicate that the AMF-TENG shows good electrical performance in the broadband frequency range from 15 to 70 Hz. Under the vibration condition of 40 Hz and 30 m/s^2, it can generate a maximum power density of 622.59 W/m^3, which is higher than previous studies by 155.2%. Finally, the AMF-TENG is proven to power temperature and humidity sensors continuously under actual machine vibration. In brief, the AMF-TENG provides a new method for efficiently scavenging of vibration energy in the broadband frequency range.

1. Introduction

The rapid development of the internet of things (IoT) has led to massive wireless sensor nodes widely distributed in different fields [1–3]. However, the traditional cable power supply faces challenges to power the distributed wireless sensor nodes due to high costs, complex distribution, electromagnetic interference, and power loss [4]. Alternatively, the battery, as another power source, requires to be recharged or replaced by regular maintenance because of the limited lifetime, which is a great difficulty in environments such as remote regions, enclosed spaces, and underwater, etc [5,6]. Thus, it is a great demand to develop high performance environmental energy harvesters for powering the distributed sensors [7,8]. Vibration, which is regarded as sustainable and clean energy, is omnipresent in industrial and social fields [9–11], such as engines [12], aircraft [13], bridges [14], buildings [15], and so forth. Vibration energy scavenging provides an alternative method to power the electronics or sensor nodes [16–18]. The majority of vibration energy has the broadband frequency and low amplitude characteristics due to the influence of environmental excitation [19–21]. Therefore, an intensive study on the efficient scavenging of vibration energy in the broadband frequency range is vital for the development of IoT.

The triboelectric nanogenerator (TENG) was invented by Zhonglin Wang and his co-workers [22–24]. Many researchers have devoted to scavenging vibration energy through TENG due to its high power density, low cost, high adaptability, and so on [25–27]. Among them, the resonant structure, which mainly relies on spring or cantilever, is one of the most popular structures [9,28]. Ren et al. [10] proposed a cantilever-structure TENG to convert low-frequency vibration sources with a frequency range from 1 to 22 Hz into electrical energy. The

* Corresponding authors.
E-mail addresses: dutaili@dlmu.edu.cn (T. Du), xuminyi@dlmu.edu.cn (M. Xu).
[1] These authors contributed equally to this work.

https://doi.org/10.1016/j.nanoen.2023.108182
Received 7 December 2022; Received in revised form 3 January 2023; Accepted 5 January 2023
Available online 6 January 2023

cantilever-structure TENG can reach an output power of 62.2 W/m^3 under the vibration frequency of 5 Hz. To broaden the frequency band of TENG, Qi et al. proposed a tandem spring-mass structure TENG to collect the vibration energy at a broadband frequency range from 3 to 45 Hz [29]. These TENGs improve the conversion efficiency and working bandwidth of vibration energy scavenging but can produce high-performance output only at the resonant frequencies. Besides, the membrane structure TENG is designed to address this issue. The VS-TENG proposed by Zhao et al. [30] is effectively applied to sense vibration frequencies from 1 to 2000 Hz, which motivates a new orientation in broadband vibration energy scavenging. However, due to the mass inertia of conventional membrane structures have low mass inertia which vibrates with small amplitude under external excitation. Therefore, it remains challenging to improve the efficiency of harvest vibration energy in broadband frequency range to sustainably power the electronics [31].

In this work, an additional mass enhanced film structure triboelectric nanogenerator (AMF-TENG) is proposed for efficiently scavenging broadband vibration energy. The additional mass is used to increase the mass inertia of the FEP film, which greatly amplifies amplitude of the AMF-TENG. From the perspective of energy conversion, the motion process of AMF-TENG is analyzed and the equivalent model is established. The main structural parameters of the AMF-TENG including the area of the FEP film and the weight of the additional mass are optimized to improve the electrical performance of the AMF-TENG. Then the vibration energy scavenging performance of the AMF-TENG is dependent on various excitations conditions, including amplitudes, frequencies, and accelerations was systematically studied. The experimental results reveal that the maximum output power density of the AMF-TENG is 622.59 W/m^3, which occupies the first place in vibration energy scavenging to the best of our knowledge. More importantly, the AMF-TENG exhibits the advantage of scavenging vibration energy in wide broadband frequency range from 5 to 80 Hz. Finally, the AMF-TENG has been demonstrated as an excellent vibration energy scavenger (VES) in the application of continuously powering a temperature and humidity sensor under actual machine vibration. The AMF-TENG has shown exceptional application potential as a power source for sensors.

2. Results and discussion

2.1. Structure and working principle of the AMF-TENG

The application scenarios, structure, and working principle of the AMF-TENG are shown in Fig. 1. As demonstrated in Fig. 1**a**, the AMF-TENG has the potential to be an efficient VES for powering sensor nodes in various fields such as ships, airplanes, and mechanical

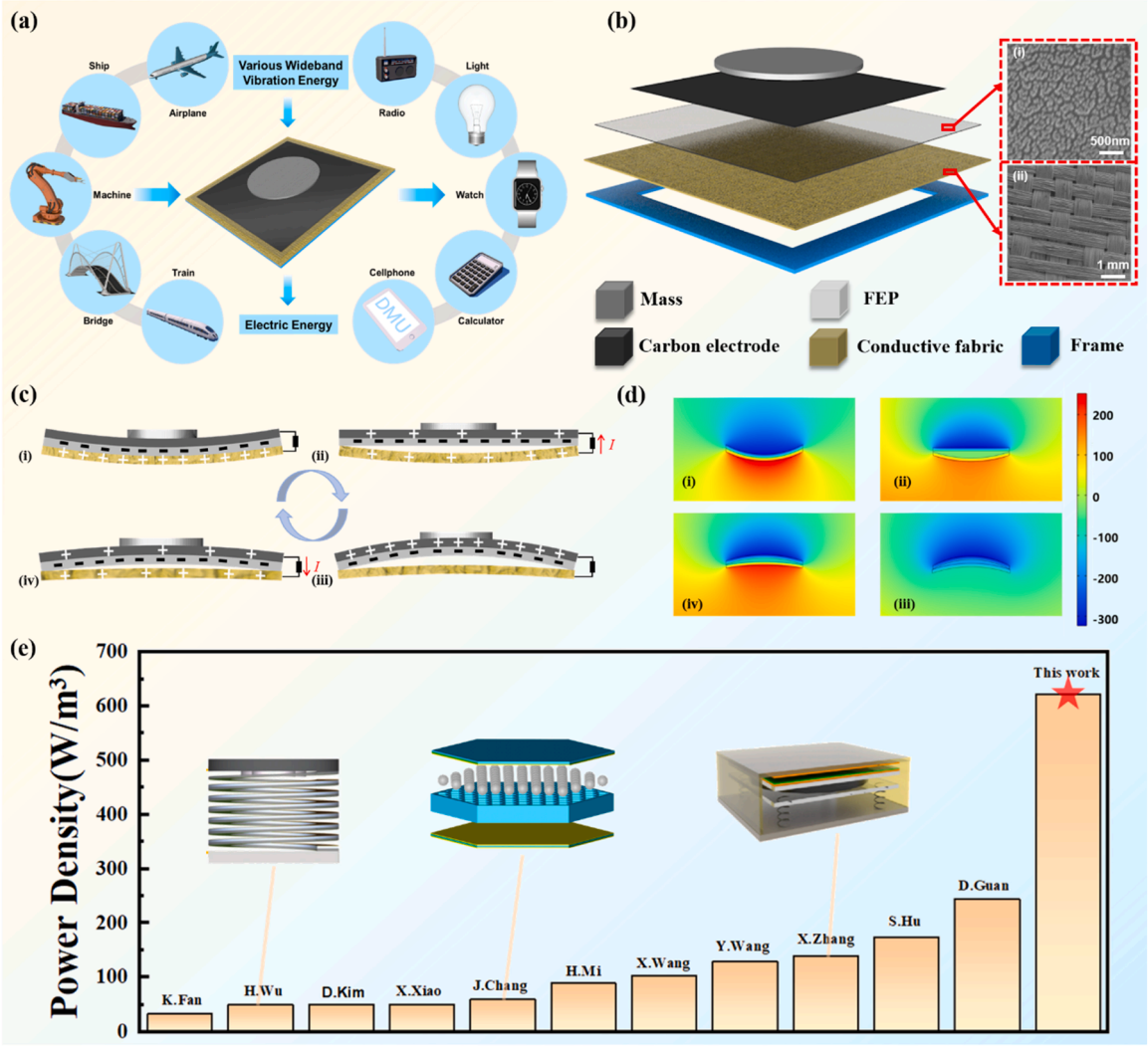

Fig. 1. Application scenarios and working principle of the AMF-TENG. (a) Application scenarios of the AMF -TENG. **(b)** Structure scheme of the AMF -TENG, scanning electron microscopy (SEM) image of **i**) the FEP film and **ii**) the conductive fabric. **(c)** Working principle of the AMF-TENG. **(d)** The potential change between the FEP film and conductive fabric by COMSOL. **(e)** Comparison of the power density with the previous work.

equipment due to its advantage of the broadband frequency range (Fig. 1**a**). The AMF-TENG consists of an additional mass, an FEP film with carbon electrode, and a conductive fabric fixed to a hollow frame (Fig. 1**b**). The optical photograph of AMF-TENG, which is thinner than a coin, is shown in Fig. S1 (Supporting Information). The additional mass is used to increase the mass inertia of FEP film, which enlargements the amplitude under external excitation. The FEP films have strong negative electronegativity, which can generate large charges during contact and separation (C-S) with the conductive fabric. Meanwhile, as an electret material, FEP film retains massive charge on its surface after several C-S motions with the conductive fabric. The conductive ink and the conductive fabric act as electrodes to transfer electrons. The surface of the FEP film is microstructure-modified by 10000-grit sandpaper to expand the contact area with the conductive fabric, and further enhance the electrical performance of the AMF-TENG [32,33]. The voltage of AMF-TENG with untreated, microstructure-modified by 5000-grit sandpaper and 10000-grit sandpaper, respectively as shown in Fig. S2. It can be seen that the utilization of 10000-grit sandpaper makes the electrical output of AMF-TENG 1000% higher than the untreated. The corresponding (SEM) images of the sanded FEP film and the conductive fabric are displayed in Fig. 1**b(i&ii)**. The conductive fabric exhibits excellent permeability benefited from its porous surface structure. The effect of the permeability of conductive fabric on the output performance of the AMF-TENG will be discussed in the following sections.

Fig. 1**c** depicts the working principle of the AMF-TENG. In the original state, the FEP film contacts with conductive fabric under the effect of additional mass. The equal positive and negative charges are generated on the surface of the FEP film and conductive fabric respectively due to the electro-negativity difference, which is shown in Fig. 1**c (i)**. As illustrated in Fig. 1**c(ii)**, the FEP film and additional mass move upward and separate from the conductive fabric. During this procedure, to balance the potential difference between the FEP film and the conductive fabric, the electrons are transferred from the carbon electrode to the conductive fabric. The electric field reaches a newly balanced as the FEP film rises to the highest position, thus the charge transfer is stopped (Fig. 1**c(iii)**). Then the electron transfer begins to reverse as the FEP film moves downward (Fig. 1**c(vi)**). Finally, the FEP film and the conductive fabric contact again with the electrical charge distribution returning to its initial state (Fig. 1**c(i)**). To verify the electric-generation principle of the AMF-TENG, the potential variation of the AMF-TENG under different working conditions is simulated using the COMSOL Multiphysics software (Fig. 1**d**), which is consistent with the above analysis.

The power density, as an important parameter, essentially reflects the output performance of the AMF-TENG. At present, plenty of VES based on TENG have been reported. The detailed information on the output performance of these TENG's vibration energy scavenging devices is presented in Table S1. As shown in Fig. 1**e**, the volumetric power density of several TENG for broadband vibration energy scavenging from previous studies are listed and compared [4, 11, 34–39], it shows

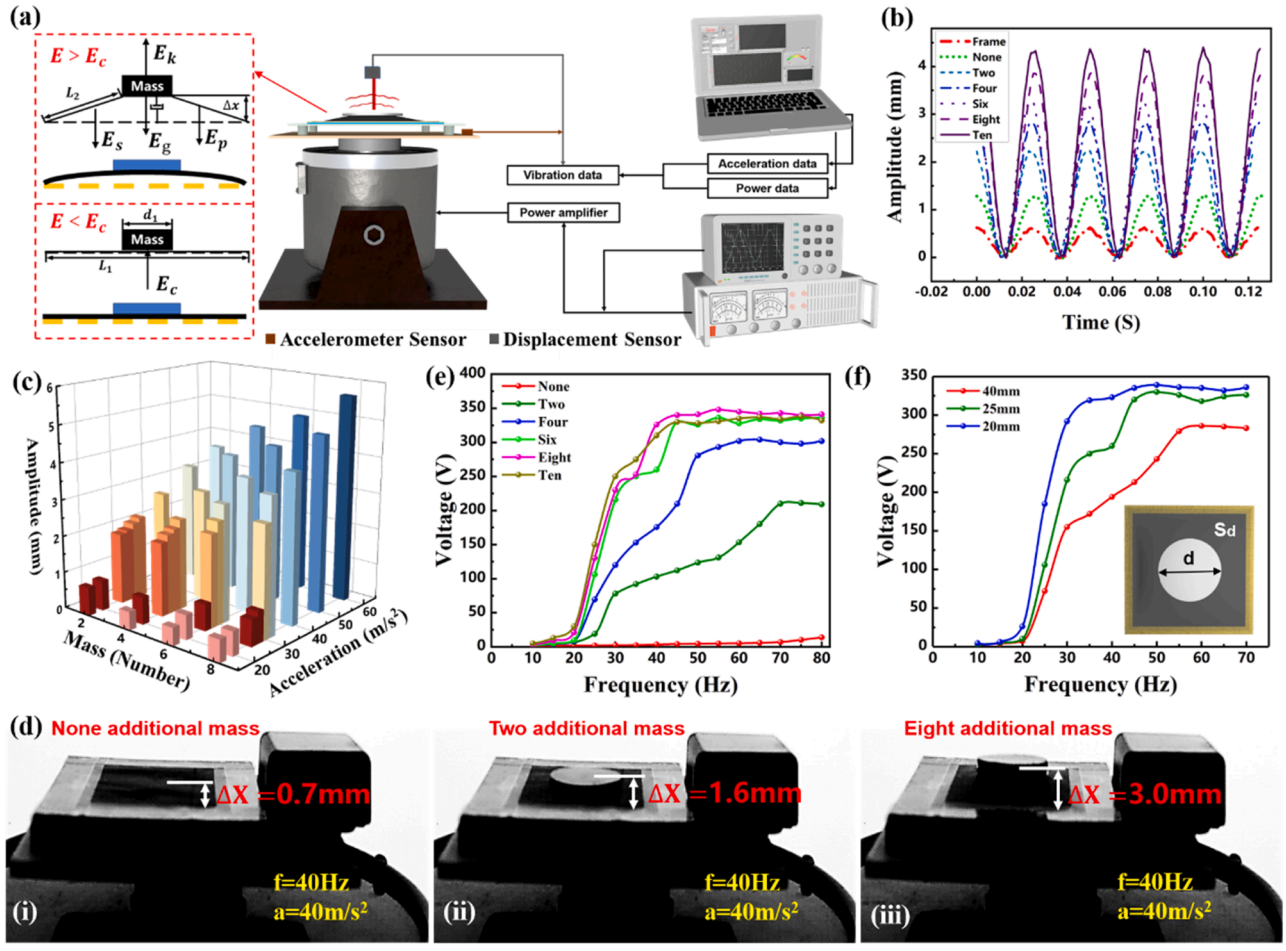

Fig. 2. Kinematic characteristics and effect of the additional mass on the performance of the AMF-TENG. (a) The theoretical model of the AMF-TENG and schematic diagram of experimental platform. **(b)** The amplitude variation curves of FEP film with different numbers of the additional mass. **(c)** Influence of acceleration and additional mass numbers on the amplitude of FEP film. **(d)** The maximum displacement of the FEP film with a different number of additional mass taken with the high-speed camera at the frequency of 40 Hz and acceleration of 40 m/s^2. **(e)** The open-circuit voltage (V_{oc}) of the AMF-TENG is dependent on the number of additional masses and **(f)** different additional mass sizes under different frequency.

that the AMF-TENG has a good performance of higher power output. Specifically, AMF-TENG generates the maximum power density of 622.59 W/m^3, which is higher than the previous literature to our best knowledge by 155.2%, where the area of the AMF-TENG is 50 × 50 mm and the height is 4.3 mm. Therefore, benefiting from the improvement of the AMF-TENG performance, this work provides an important demonstration of the excellent vibration energy collection by TENG.

2.2. Kinematic characteristics with different additional mass

To investigate the kinematic characteristics and output of the AMF-TENG, an experimental platform is constructed as shown in Fig. 2**a**. The AMF-TENG is mounted on a shaker with the amplitude and frequency precisely adjusted through the power amplifier and function signal generator, respectively. The acceleration sensor is fixed to the shaker to measure the vibration acceleration. The displacement of FEP films with additional mass is measured by a laser displacement sensor. The shaker can generate sinusoidal excitation, hence the frequency (f), amplitude (A), and maximum vibration acceleration (a_m) are the most common characteristic parameters to represent vibration excitation, which are defined by the following expressions:

$$y_b = A\sin(\omega t + \varphi) \tag{1}$$

$$a_m = A\omega^2 = A(2\pi f)^2 \tag{2}$$

y_b is the simple harmonic motion function of the external excitation, ω is the angular velocity. As shown in Fig. 2**a**, the motion of additional mass can be divided into two different conditions as the frame vibrates to maximum displacement from the perspective of energy conversion. The additional mass vibrates downward with the frame when the energy (E) of vibration is less than critical mechanical energy (E_c). The E_c with which the additional mass can separate from the conductive fabric can be expressed as:

$$E_c = \int_0^A m_0 \bullet a(\gamma)d\gamma = \frac{1}{2} m_0 \bullet a_m \bullet A \tag{3}$$

here m_0 is the weight of the additional mass, and γ is the vibration displacement. And additional mass continues to move upward by the force of inertia when the vibration energy is greater than E_c. At this point, the E_c of the additional mass consists of four parts including the kinetic energy (E_k), gravitational potential energy (E_g), elastic potential energy of the FEP film (E_p) and the energy loss (E_l) generated by mutual collision and friction between FEP film and conductive fabric. Thus, the energy conservation equation can be written as: $E = E_k + E_g + E_p + E_l$, the gravitational potential energy obtained by the additional mass can be given as $E_g = m_0 \bullet g \bullet 2(A + \Delta x)$. Where Δx is the relative displacement of additional mass to the conductive fabric. Since the vibration of the additional mass is limited by the FEP film, considering the vibration characteristic of the FEP film, Δx can be expressed as [30]:

$$\Delta x = \frac{m_0 a_m}{m\sqrt{\left(\omega_0{}^2 - \omega^2\right)^2 + 4\left(\frac{m^2}{\alpha^2} + \omega^2\right)}}\cos(\omega t - \varphi) \tag{4}$$

here m is the mass of FEP film, α is the damping coefficient from the air which is influenced by the permeability of the frame, and ω_0 is the angular frequencies of FEP film. The E_k of additional mass can expression of $E_k = \frac{m_0 \bullet v^2}{2}$, where v is the velocity of the additional mass as it leaves the frame. The elastic potential energy of the FEP film due to deformation is $E_p = \int_{\Delta l}^{0} -kxdx = \frac{1}{2}k\left((\Delta x^2 + \frac{(L_2 - d_2)}{2})^2 - L_1\right)^2$, where k is the elasticity coefficient of the FEP film, L_1 is the length of FEP film, d_2 is the diameter of the additional mass, andL_2 is the side length of the frame. When the additional mass moves to the maximum displacement, all E_k is converted into potential energy, and the E_l can be neglected (i.e., $E_l = 0$). Thus, there is the following equation:

$$m_0 a_m A = m_0 g\Delta x + \frac{1}{2}k\left(\left(\Delta x^2 + \frac{(L_2 - d_2)}{2}\right)^2 - L_1\right)^2 \tag{5}$$

As mentioned above, the motion of the additional mass is affected by the weight and area of additional mass, size of FEP film, shape of frame, and external vibration, which will be investigated in further experiments. The additional mass improves the inertia of the FEP film, resulting in the increase of the amplitude of the FEP film. Fig. 2**b** shows the effect of additional mass on the vibration amplitude of the FEP film at $f = 40$ Hz and acceleration of 40 m/s^2. The weight of additional mass is changed by adjusting the numbers. Specifically, the parameters of the different additional mass sizes are shown in Fig. S3. The displacement of the frame and the FEP film with different numbers of additional mass is measured by laser displacement sensors. As shown in Fig. 2**b**, the amplitude of FEP film amplifies with the weight of the additional mass. And the amplitude of FEP film with ten additional mass attached is 5.2 mm, which is 3.25 times larger than that without the additional mass. The amplitude of FEP film amplifies with the weight of the additional mass as the number of mass blocks exceeds 10 are shown in Fig. S4. Fig. 2**c** shows the effect of maximum acceleration and the number of additional masses on the amplitude of FEP film at the $f = 40$ Hz. The result shows that the amplitude of the FEP film increases with both the numbers of additional mass and vibration maximum acceleration. It is worth noting that as the mass number increases, the acceleration required for the FEP film to effectively separate (i.e., amplitude of FEP film greater than 1.5 mm) from the conductive fabrics gradually increases. In particular, the acceleration of FEP film to effectively separate from the conductive fabrics increases from 20 m/s^2 to 28 m/s^2 when the number of additional mass increases from 2 to 8, which has little effect on the start-up acceleration of the TENG. The reason is that the FEP film with more additional mass attached needs more energy to overcome gravity to move. To further clearly demonstrate the effect of weight on FEP film displacement. As shown in Fig. 2**d**, the moving characteristics of the FEP film were verified through utilizing a high-speed camera at $f = 40$ Hz and acceleration of 40 m/s^2. Fig. 2**d(iii)** clearly shows the relative displacement (Δx) of the FEP film with eight additional masses attached is 3.0 mm which is much larger than that without additional mass. The experimental trend analyzed through the high-speed camera is consistent with that mentioned above. More details on the moving characteristics of the FEP film can be seen in Supplementary Movie S1. In addition, the V_{oc} of the AMF-TENG dependent on the numbers of additional mass is investigated at the $f = 50$ Hz and A = 0.5 mm as shown in Fig. S5. It can be seen that the peak voltage is 3 V while the additional mass is not applied to the FEP film. When the number of additional masses varies from 2 to 6, the V_{oc} of the AMF-TENG increases sharply from 120 V to 320 V. Then, the V_{oc} of the AMF-TENG almost remains constant as the number of the additional mass continues to increase. Fig. 2**e** shows the relationship of the V_{oc} on the excitation frequency with additional mass numbers as the A = 0.5 mm. The frequency range of vibration energy scavenges is from 10 to 80 Hz. To investigate in more detail, the V_{oc}, short-circuit current (I_{sc}), and transferred charge (Q_{oc}) of the AMF-TENG with six additional mass is discussed separately (Fig. S6). It is obvious that the process of output change can be divided into three stages. First, as the AMF-TENG is the C-S mode, the equation of electrical output for AMF-TENG is elaborated as [40,41]:

$$V_{OC} = \frac{\sigma \Delta x}{\varepsilon_0} \tag{6}$$

where V_{oc} means the open-circuit voltage, ε_0 is the dielectric constant in vacuum, σ is the charge density of FEP film. When the excitation frequency is less than 20 Hz, the additional mass cannot separate from the conductive fabrics because the energy obtained by the additional mass is not enough to overcome the effects of gravity. As a result, only a few

electrons are transferred through the external circuit. Second, V_{oc} increases rapidly from 100 V to 300 V while the excitation frequency augments from 25 Hz to 45 Hz. At this stage, the FEP film vibrates along with the additional mass. Thus, the V_{oc} of the AMF-TENG has improved due to the increase of the effective contact area. At last, V_{oc} almost remains constant (V_{oc} = 332 V), because as the excitation frequency varies from 45 to 80 Hz, the effective contact area remains the maximum. The current and transferred charge have a similar trend. The experimental result indicates that the AMF-TENG is capable of scavenging vibration energy in the broadband frequency range. Besides, as shown in Fig. 2**e**, the peak *Voc* of the AMF-TENG without additional mass is only 13 V at the frequency of 80 Hz, with the application of additional mass increasing V_{oc} by 25.5 times (i.e., V_{oc} =332 V). Meanwhile, the V_{oc} of above three stage is dependent on the numbers of additional mass. In the first, the weight of the additional mass almost has hardly affected the V_{oc}. While the V_{oc} increases dramatically as the number of the additional mass varies from 0 to 10 (second stage). In the third stage, the V_{oc} almost remains constant regardless of the additional mass numbers as the vibration frequency increases. However, it is noticed that the value of the frequency that the optimum of V_{oc} appears to reduce from 80 to 35 Hz with the increase of the additional mass number from 0 to 10. And the additional mass number almost has no effect on the V_{oc} of the AMF-TENG as the number changes from 6 to 10. The reason can be explained that both the effective contact area and the effect of displacement reach the maximum as the additional mass number varies from 6 to 10. According to Eq (5), the additional mass area is also an essential factor that influences the electrical output performance of AMF-TENG. Fig. 2**f** shows the V_{oc} of the AMF-TENG varies with different diameters of additional mass with the fixed weight of 6.8g as the excitation frequency augments from 10 to 80 Hz. Meantime, to provide sufficient deformation area (S_d) for the membrane, the additional mass has a maximum diameter of 40 mm and a minimum diameter of 20 mm. The V_{oc} of the AMF-TENG increases as the diameter of the additional mass reduces from 40 to 20 mm. Fig. S7 compares the V_{oc} of AMF-TENG as the additional mass diameter (d_1) is 20, 25, and 40 mm (f = 50 Hz and A = 0.5 mm). It is obvious that the V_{oc} decreases with the expanded area of additional mass. As Fig. S8 shows the amplitude of FEP film decreases with the increase of additional mass diameter. This result is that the increase in the additional mass area reduces the S_d of the FEP film, which results in a smaller vibration amplitude. Thus, the optimized additional mass number and diameter of 6 and 25 mm are applied for further experimental study, respectively.

Supplementary material related to this article can be found online at doi:10.1016/j.nanoen.2023.108182.

2.3. Effect of structural parameters

To investigate the effect of the permeability of the supporting frame on the V_{oc} of the AMF-TENG, we constructed three types of frames (with an area of 50 ×50 mm) including hollow, hole, and enclosed as shown in Fig. 3**a**. The AMF-TENG with the hollow frame has the largest vibration amplitude of 6.3 mm at the f = 40 Hz compared with the other types of frames as shown in Fig. 3**b**. It is obvious that the amplitude of FEP film can be improved by optimizing the permeability of the frames. The reason may be that the vibration of the additional mass leads to changes in the air pressure between the FEP film and the conductive fabrics, which is influenced by the frame permeability. According to Eq. (4), the improvement of the frame permeability can enhance the damping coefficient, thereby the amplitude of the FEP film is improved. Then, the V_{oc} of the AMF-TENG dependent on the various types of frames is investigated as shown in Fig. 3**c**. The V_{oc} of the hollow, hole and enclosed frames is 149 V, 160 V, and 180 V at the f = 40 Hz, indicating that the improvement of the frame permeability can increase the electrical performance of the AMF-TENG. In order to further understand the effect of permeability, V_{oc} of the AMF-TENG dependent on the frequency with the different types of frames is studied under the fixed amplitude of

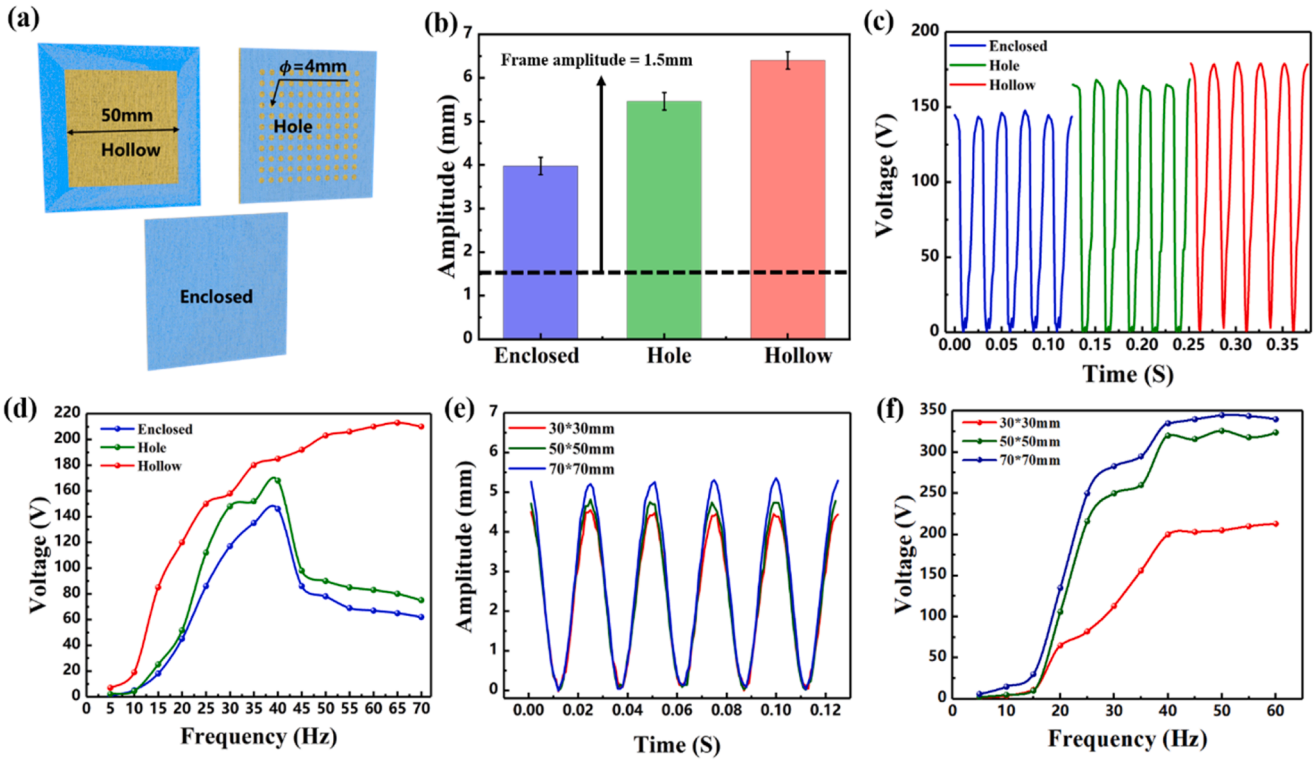

Fig. 3. Effect of frame type and film area on AMF-TENG. (a) Schematic diagram of various types of frames including hollow, hole and enclosed frame. **(b)** The amplitude of FEP films is dependent on the different types of frames. **(c)** The V_{oc} of the AMF-TENG is dependent on the different types of frames at the f = 40 Hz. **(d)** The V_{oc} of the AMF-TENG is dependent on the vibration frequency under various types of frames. **(e)** The amplitude of FEP films is dependent on the different areas of FEP film. **(f)** The V_{oc} of the AMF-TENG is dependent on the vibration frequency under various areas of FEP film.

0.5 mm. As shown in Fig. 3**d**, the application of the hollow frame can improve the output performance of the AMF-TENG. As the frequency exceeds 50 Hz, the V_{oc} of the hollow frame stabilizes at about 200 V, which is 150% higher than that of the enclosed frame. Both the hole and enclosed frames reach the peak V_{oc} at the $f = 40$ Hz. Then the V_{oc} drops rapidly as the frequency increases from 40 Hz to 70 Hz. The experimental result indicates that the hollow frame can efficiently collect the vibration energy in a wider range of frequencies.

According to Eq. (5), the area of the FEP film also plays a vital role in determining the electrical output of AMF-TENG. Therefore, the influence of the FEP film area on working performance was systematically studied. The amplitude of FEP film increases with the enlargement of the area, as shown in Fig. 3**e**. The reason for this phenomenon is that the enlargement of the film area reduces the elastic potential energy (E_p) that the mass needs to consume when it vibrates upward. And more kinetic energy (E_k) is converted into gravitational potential energy (E_g), thereby the vibration amplitude of the FEP film increases. As shown in Fig. 3**f,** the V_{oc} of AMF-TENG increases with the area of the FEP film. As the area of the FEP film increases from 30 × 30 mm to 50 × 50 mm, the V_{oc} of AMF-TENG improved from 201 to 328 V. However, the V_{oc} increases from 328 to 345 V as the FEP film area increases from 50 × 50 mm to 70 × 70 mm. Since the area of FEP film has a lesser effect on the electrical output of AMF-TENG as the area exceeds 50 × 50 mm, the film area of 50 × 50 mm is used for further experiments.

2.4. Output performance under various external excitation conditions

To explore the working performance of the AMF-TENG under various external excitation, the effect of main excitation parameters on the electrical output is investigated. Fig. 4**a** depicts the relationship between the excitation parameters (i.e., frequency (f), amplitude (A), and maximum acceleration (a_m)). As shown in Fig. 4**b, c, and** Fig. S9, the V_{oc}, I_{sc}, and Q_{oc} of the AMF-TENG increase from 8.3 V, 1 μA, 5.1 nC to 344 V, 43.5 μA, 166 nC as the amplitude of external excitation increases from 1.2 to 5.0 mm. This phenomenon is that the increase of amplitude leads to a larger displacement distance (Δx) and acceleration (a_m) according to Eq. (4). Then, the effect of the frequency of external excitation on the electrical performance of the AMF-TENG is studied at the acceleration of 20 m/s^2. As shown in Fig. 4**d**, the V_{oc} of the AMF-TENG reaches 320 V at the $f = 45$ Hz. Then the electrical output of the AMF-TENG decreases with the frequency varying from 45 Hz to 70 Hz. The reason

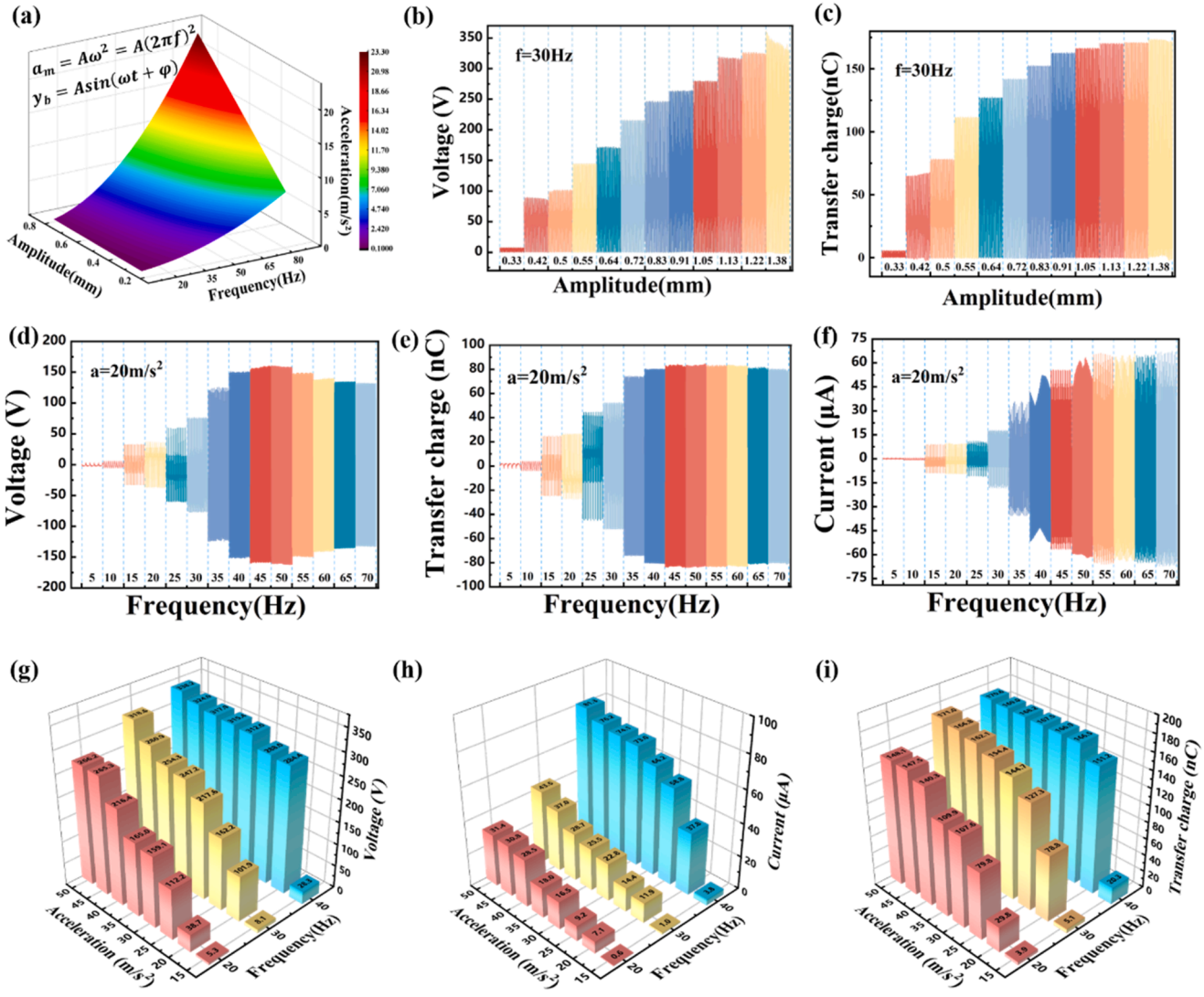

Fig. 4. Output performance of AMF-TENG under various excitation. (a) The maximum excitation acceleration is dependent on the amplitude and frequency. **b)** V_{oc} and **c)** Q_{oc} of the AMF-TENG dependent on the various amplitudes at $f = 30$ Hz. **d)** The V_{oc}, **e)** Q_{oc}, and I_{sc}. **f)** of the AMF-TENG dependent on the various frequencies as the acceleration of 20 m/s^2. **g)** V_{oc}, **h)** I_{sc}, and **i)** Q_{oc} of the AMF-TENG dependent on the various acceleration as the frequency of 20 Hz, 30 Hz, and 40 Hz.

for this phenomenon is that the V_{oc} is influenced by both the (Δx) and Q_{oc}. According to Eq. (2), the amplitude decreases with increasing frequency as the acceleration is fixed. However, the Q_{oc} increases from 5 nC to 168 nC as the frequency varies from 5 to 45 Hz as shown in Fig. 4**e**, which results from the enlarging of the effective contact area between the FEP film and conductive fabrics. Then the Q_{oc} almost remains constant while the frequency continues to increase, indicating the contact area has achieved the maximum. Therefore, the V_{oc} of AMF-TENG is optimal at the f = 45 Hz and then decreases. As shown in Fig. 4**f**, the I_{sc} of the AMF-TENG is enhanced from 0.7 μA to 66 μA with the frequency varying from 5 to 70 Hz, which can be attributed to the increase of both Q_{oc} and the frequency. More notably, the minimum values of V_{oc}, I_{sc}, and Q_{oc} generated by AMF-TENG are 66 V, 9.2 μA, and 50 nC in a frequency range from 15 to 70 Hz, which indicates that the AMF-TENG can generate electrical output in a broadband frequency range.

Fig. 4 **g-i** shows the V_{oc}, I_{sc}, and Q_{oc} of AMF-TENG dependent on the vibration acceleration and the frequency, respectively. The V_{oc}, I_{sc}, and Q_{oc} of the AMF-TENG are improved as the excitation frequency is enhanced from 20 to 40 Hz at the fixed acceleration, which is consistent with the experimental trend above. Besides, the output performance of the AMF-TENG improves with the excitation acceleration at the fixed frequency. The reason can be explained that the amplitude of FEP film increases with the excitation acceleration under the constant frequency according to Eq. (2). It is believed that the AMF-TENG exhibits a great perspective as a VES in many fields due to the merit of high adaptability in frequency.

2.5. Demonstration of the AMF-TENG

Based on the excellent performance of the AMF-TENG studied above, to further demonstrate the application of AMF-TENG as a VES. As shown in Fig. 5**a**, as the I_{sc} of AMF-TENG decreases with the rise of resistance, the output power density of 622.59 W/m^3 is maximized while the resistance of 4 MΩ. Then the AMF-TENG is applied as a VES to charge the various capacitors. As shown in Fig. 5**b**, different capacitors are charged to 3 V by TENG, although the time required for charging increases as the amplify of capacitor value, the 1000 μF capacitor only requires about 300 s to be charged to 3 V, which indicates that AMF-TENG has excellent performance to charge the capacitors.

To verify the durability of AMF-TENG, the V_{oc} of the AMF-TENG is tested under the fixed vibration acceleration of 40 m/s^2 for 3 continuous weeks. As shown in Fig. 5**c**, the V_{oc} is almost invariable, indicating the robustness and sustainability of AMF-TENG. As shown in Fig. 5**d** and Supplementary Movie S2, a temperature and humidity sensor is capable of continuous operation after a 1000 μF capacitor is charged to 3 V by the AMF-TENG. The detailed power management circuit is shown in Fig. 5**e**, to power the electronics requiring direct current input, the electricity generated by the AMF-TENG should be rectified by a rectifier bridge to charge a capacitor. The Fig. 5**f** and Supplementary Movie S3 illustrate that the AMF-TENG is successfully demonstrated to light up

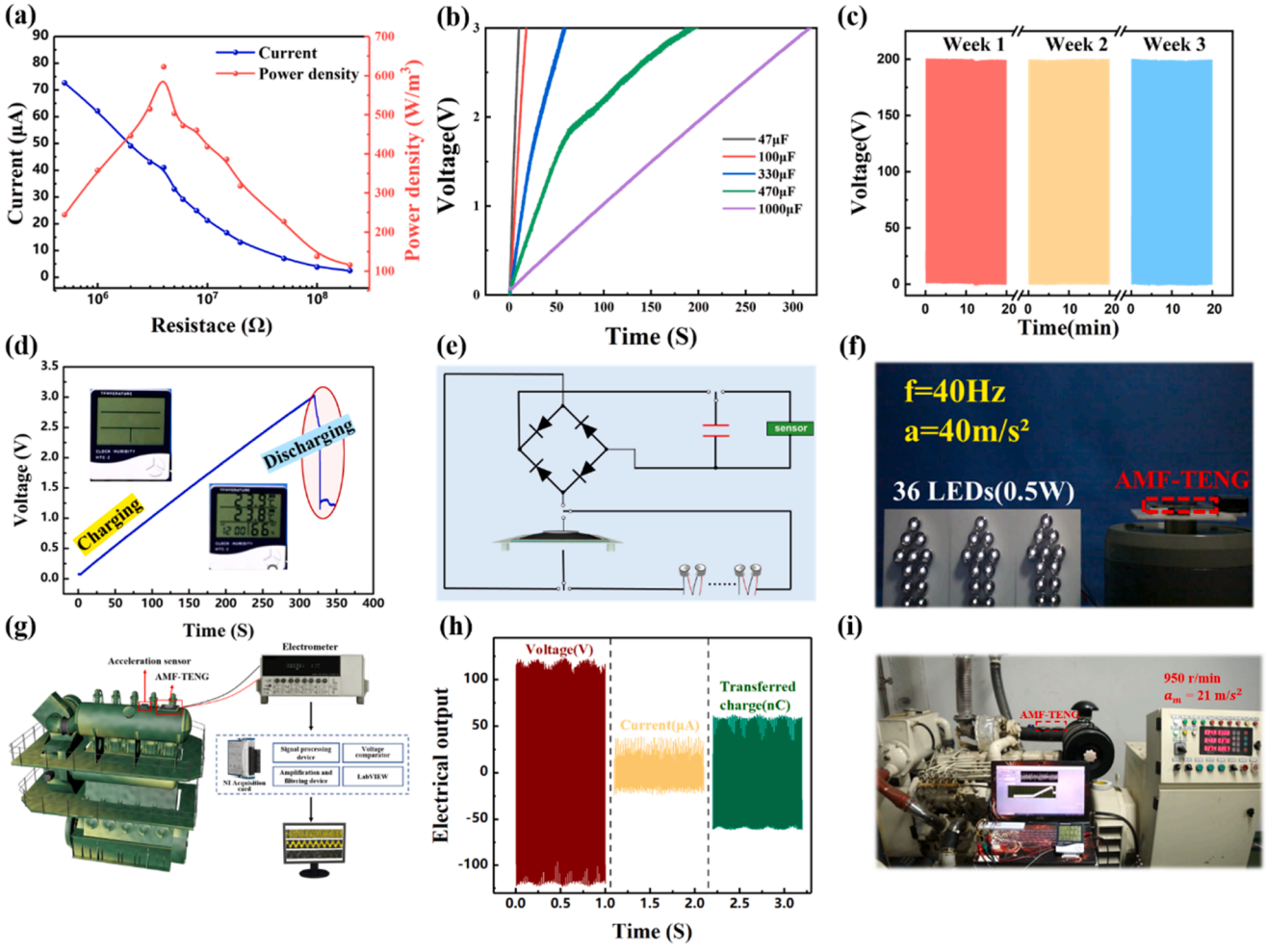

Fig. 5. Application the AMF-TENG. (a) Effect of the load resistance on the current and power density at the f = 40 Hz and acceleration of 30 m/s^2 **(b)** Charging performance of the AMF-TENG. **(c)** The durability of AMF-TENG. **(d)** A temperature and humidity sensor continuously powered by AMF-TENG. **(e)** The working circuit of AMF-TENG. **(f)** 36 × 0.5 W LEDs are lit up simultaneously by AMF-TENG. **(g)** Experimental schematic, (h) electrical output performance, and (g) demonstration of AMF-TENG powering a temperature and humidity sensor under actual machine vibration.

36 × 0.5 W LEDs connected in series, which indicates that the AMF-TENG is capable of continuously powering the electronics. To further investigate the electrical output performance of AMF-TENG under actual machine vibration, as shown in Fig. 5**g** the AMF-TENG is fixed to the air inlet pipe of diesel engine (the model is 6BT5.9-GM83 and rate at 950 rpm/min) that can generate an external excitation of 21 m/s^2 and the test platform was constructed. Fig. 5**h** shows the values of voltage, current and charge generated by AMF-TENG under actual machine vibration are 270 V, 30 μA, and 120 nC, which indicates that the AMF-TENG has excellent electrical output performance under actual machine vibration. As shown in Fig. 5**i** and Supplementary Movie S4, the AMF-TENG is proven to power temperature and humidity sensors continuously under actual machine vibration. In brief, the AMF-TENG provides a new method for efficiently scavenging vibration energy under actual machine vibration to continuously powering the sensor.

Supplementary material related to this article can be found online at doi:10.1016/j.nanoen.2023.108182.

Supplementary material related to this article can be found online at doi:10.1016/j.nanoen.2023.108182.

Supplementary material related to this article can be found online at doi:10.1016/j.nanoen.2023.108182.

3. Conclusion

In summary, an additional mass film structure triboelectric nanogenerator has been developed and investigated for scavenging broadband vibration energy with the merits of simple structure, small volume, and high power density. To explore its working mechanism, the theoretical model of AMF-TENG is created. The electrical output of the AMF-TENG is efficiently improved by optimizing the main structural parameters, such as the number, area of the additional mass, and the permeability of the supporting frame, etc. The experimental results indicate that additional mass can improve the amplitude of the FEP membrane by 3.4 times, which enhances the V_{oc} by 25.5 times, and with the utilization of hollow frame, the V_{oc} of AMF-TENG is 150% higher than the enclosed frame. Further, the output performance of AMF-TENG under various vibration conditions was systematically investigated. The AMF-TENG shows good electrical performance in broadband frequency range from 15 to 70 Hz. The output of AMF-TENG augments gradually with the excitation amplitude and acceleration. The AMF-TENG can generate a maximum power density unit volume of 622.59 W/m^3. Finally, the AMF-TENG has been demonstrated lighting the 36 × 0.5 W commercial LEDs and powering a temperature and humidity sensor continuously under actual machine vibration. Therefore, the AMF-TENG has exceptional potential application in broadband vibration energy scavenging fields.

4. Experimental section

4.1. Fabrication of AMF-TENG

The AMF-TENG consists of additional mass, an FEP film (30μm), a conductive fabric, and a frame (1 mm in thickness) printed by a 3D printer. The additional mass is fixed to the FEP film by using insulating double-sided tape, which is used to avoid the performance of the electrodes being affected. Copper wires have adhered to the conductive fabric and conductive ink respectively as signal acquisition lines. The frames were compared using three models: enclosed, hole, and voided. Conductive fabrics and FEP films were tested with areas of 30 × 30 mm, 50 × 50 mm, and 70 × 70 mm. The additional mass with diameters of 20, 25, and 40 mm and different quantities were used for the experiments.

4.2. Observation of movement of the film

The motion of FEP film is observed by applying a high-speed camera (PHANTOM V2012:20–28 VDC INPUT-10 AMP MAX@24VDC) and PCC 3.7 software. The vibration displacement of the FEP film is observed by a laser displacement sensor (HG-C1100) and Keithley 6514 electrostatic meter.

4.3. Electrical output measurements

The AMF-TENG is fixed to an electrodynamic shaker (JZK-20) with the frequency and amplitude regulated by a functional signal generator (YE1311) and an amplifier (YE5852), respectively. Acceleration is measured by a commercial smart 6-axis Bluetooth 2.0 accelerometer (BWT61CL) and real-time display on the computer through MinilMU software. The electric output signals (V_{oc}, I_{sc}, and Q_{oc}) were measured by an electrometer (Keithley 6514).

CRediT authorship contribution statement

Hongyong Yu: Investigation, Software, Data curation, and Writing – review and editing. **Ziyue Xi:** Conceptualization, Software, and editing. **Yiping Zhang:** Data curation, Software. **Ruijiang Xu:** Data curation and Software. **Cong Zhao:** Investigation and Visualization. **Yawei Wang:** Investigation and Visualization. **Xinyang Guo:** Visualization. **Yue Huang:** Visualization. **Jianchun Mi:** Visualization. **Yejin Lin:** Visualization. **Taili Du:** Conceptualization, Methodology and Writing – review. **Minyi Xu:** Conceptualization, Methodology and Writing – review.

Declaration of Competing Interest

The authors declare that they have no known competing financial interests or personal relationships that could have appeared to influence the work reported in this paper.

Data availability

Data will be made available on request.

Acknowledgments

This work was supported by the National Key R & D Project from the Minister of Science and Technology (Grant No. 2021YFA1201604), the National Natural Science Foundation of China (Grant No.51879022, 52101345), the Dalian Outstanding Young Scientific and Technological Talents Project (Grant No.2021RJ11), Application Research Program of Liaoning Province (Grant No. 2022JH2/01300219), Scientific Research Fund of the Educational Department of Liaoning Province (Grant No. LJKZ0055), and Fundamental Research Funds for the Central Universities (Grant No.3132022211).

Appendix A. Supporting information

Supplementary data associated with this article can be found in the online version at doi:10.1016/j.nanoen.2023.108182.

References

[1] X. Luo, L. Zhu, Y.C. Wang, J. Li, J. Nie, Z.L. Wang, A flexible multifunctional triboelectric nanogenerator based on MXene/PVA hydrogel, Adv. Funct. Mater. 31 (2021), https://doi.org/10.1002/adfm.202104928.

[2] J. Luo, W. Gao, Z.L. Wang, The triboelectric nanogenerator as an innovative technology toward intelligent sports, Adv. Mater. 33 (2021), e2004178, https://doi.org/10.1002/adma.202004178.

[3] X. Ma, S. Zhou, A review of flow-induced vibration energy harvesters, Energy Convers. Manag. 254 (2022), https://doi.org/10.1016/j.enconman.2022.115223.

[4] D. Guan, G. Xu, X. Xia, J. Wang, Y. Zi, Boosting the output performance of the triboelectric nanogenerator through the nonlinear oscillator, ACS Appl. Mater. Interfaces 13 (2021) 6331–6338, https://doi.org/10.1021/acsami.0c21246.

[5] Y. Wang, X.Y. Liu, Y.W. Wang, H. Wang, H. Wang, S.L. Zhang, T.C. Zhao, M.Y. Xu, Z.L. Wang, Flexible seaweed-like triboelectric nanogenerator as a wave energy

harvester powering marine internet of things, ACS NANO 15 (2021) 15700–15709, https://doi.org/10.1021/acsnano.1c05127.
[6] Y. Wang, Z. Qian, C. Zhao, Y. Wang, K. Jiang, J. Wang, Z. Meng, F. Li, C. Zhu, P. Chen, H. Wang, M. Xu, Highly adaptive triboelectric-electromagnetic hybrid nanogenerator for scavenging flow energy and self-powered marine wireless sensing, Adv. Mater. Technol. (2022), https://doi.org/10.1002/admt.202201245.
[7] H. Zhao, X. Xiao, P. Xu, T. Zhao, L. Song, X. Pan, J. Mi, M. Xu, Z.L. Wang, Dual-tube helmholtz resonator-based triboelectric nanogenerator for highly efficient harvesting of acoustic energy, Adv. Energy Mater. 9 (2019), https://doi.org/10.1002/aenm.201902824.
[8] M.Y. Xu, T.C. Zhao, C. Wang, S.L. Zhang, Z. Li, X.X. Pan, Z.L. Wang, High power density tower-like triboelectric nanogenerator for harvesting arbitrary directional water wave energy, ACS NANO 13 (2019) 1932–1939, https://doi.org/10.1021/acsnano.8b08274.
[9] J. Yang, J. Chen, Y. Yang, H. Zhang, W. Yang, P. Bai, Y. Su, Z.L. Wang, Broadband vibrational energy harvesting based on a triboelectric nanogenerator, advanced energy, Materials 4 (2014), https://doi.org/10.1002/aenm.201301322.
[10] Z. Ren, L. Wu, J. Zhang, Y. Wang, Y. Wang, Q. Li, F. Wang, X. Liang, R. Yang, Trapezoidal cantilever-structure triboelectric nanogenerator integrated with a power management module for low-frequency vibration energy harvesting, ACS Appl. Mater. Interfaces 14 (2022) 5497–5505, https://doi.org/10.1021/acsami.1c23309.
[11] H. Wu, J. Wang, Z. Wu, S. Kang, X. Wei, H. Wang, H. Luo, L. Yang, R. Liao, Z. L. Wang, Multi-parameter optimized triboelectric nanogenerator based self-powered sensor network for broadband aeolian vibration online-monitoring of transmission lines, Adv. Energy Mater. 12 (2022), https://doi.org/10.1002/aenm.202103654.
[12] M.H. Mohd Ghazali, W. Rahiman, G. Tang, Vibration analysis for machine monitoring and diagnosis: a systematic review, Shock Vib. 2021 (2021) 1–25, https://doi.org/10.1155/2021/9469318.
[13] P. Gao, T. Yu, Y. Zhang, J. Wang, J. Zhai, Vibration analysis and control technologies of hydraulic pipeline system in aircraft: a review, Chin. J. Aeronaut. 34 (2021) 83–114, https://doi.org/10.1016/j.cja.2020.07.007.
[14] L. Liang, X. Li, R. Bi, Z. Gong, Y. Sun, Investigation of the effect of vibration-reducing tracks on the vibration and noise from a large-span steel bridge, J. Vib. Control (2022), https://doi.org/10.1177/10775463221075403.
[15] X. Zou, G. Jiang, L. Ye, Vibration response analysis of a new scientific research ship based on finite element modeling, J. Mar. Sci. Appl. 21 (2022) 69–81, https://doi.org/10.1007/s11804-022-00272-z.
[16] Z.L. Wang, A.C. Wang, On the origin of contact-electrification, Mater. TODAY 30 (2019) 34–51, https://doi.org/10.1016/j.mattod.2019.05.016.
[17] M. Majid, S. Habib, A.R. Javed, M. Rizwan, G. Srivastava, T.R. Gadekallu, J.C. Lin, Applications of wireless sensor networks and internet of things frameworks in the industry revolution 4.0: a systematic literature review, Sensor 22 (2022), https://doi.org/10.3390/s22062087.
[18] O.I. Khalaf, C.A.T. Romero, S. Hassan, M.T. Iqbal, T.V. Hoang, Mitigating hotspot issues in heterogeneous wireless sensor networks, J. Sens. 2022 (2022) 1–14, https://doi.org/10.1155/2022/7909472.
[19] Y. Qi, Y. Kuang, Y. Liu, G. Liu, J. Zeng, J. Zhao, L. Wang, M. Zhu, C. Zhang, Kirigami-inspired triboelectric nanogenerator as ultra-wide-band vibrational energy harvester and self-powered acceleration sensor, Appl. Energy 327 (2022), https://doi.org/10.1016/j.apenergy.2022.120092.
[20] Y. Qi, G. Liu, Y. Kuang, L. Wang, J. Zeng, Y. Lin, H. Zhou, M. Zhu, C. Zhang, Frequency band broadening and charge density enhancement of a vibrational triboelectric nanogenerator with two stoppers, Nano Energy 99 (2022), https://doi.org/10.1016/j.nanoen.2022.107427.
[21] J. Zhao, G. Zhen, G. Liu, T. Bu, W. Liu, X. Fu, P. Zhang, C. Zhang, Z.L. Wang, Remarkable merits of triboelectric nanogenerator than electromagnetic generator for harvesting small-amplitude mechanical energy, Nano Energy 61 (2019) 111–118, https://doi.org/10.1016/j.nanoen.2019.04.047.
[22] T. Du, F. Dong, R. Xu, Y. Zou, H. Wang, X. Jiang, Z. Xi, H. Yuan, Y. Zhang, P. Sun, M. Xu, A drill pipe-embedded vibration energy harvester and self-powered sensor based on annular type triboelectric nanogenerator for measurement while drilling system, Adv. Mater. Technol. (2022), https://doi.org/10.1002/admt.202200003.
[23] Y. Wang, D. Liu, Z. Hu, T. Chen, Z. Zhang, H. Wang, T. Du, S.L. Zhang, Z. Zhao, T. Zhou, M. Xu, A triboelectric-nanogenerator-based gas–solid two-phase flow sensor for pneumatic conveying system detecting, Adv. Mater. Technol. 6 (2021), https://doi.org/10.1002/admt.202001270.
[24] Z. Song, J. Yin, Z. Wang, C. Lu, Z. Yang, Z. Zhao, Z. Lin, J. Wang, C. Wu, J. Cheng, Y. Dai, Y. Zi, S.-L. Huang, X. Chen, J. Song, G. Li, W. Ding, A flexible triboelectric tactile sensor for simultaneous material and texture recognition, Nano Energy 93 (2022), https://doi.org/10.1016/j.nanoen.2021.106798.
[25] Z. Wang, Y. Jin, C. Lu, J. Wang, Z. Song, X. Yang, Y. Cao, Y. Zi, Z.L. Wang, W. Ding, Triboelectric-nanogenerator-enabled mechanical modulation for infrared wireless communications, Energy Environ. Sci. 15 (2022) 2983–2991, https://doi.org/10.1039/d2ee00900e.
[26] H.F. Zhao, M.Y. Xu, M.R. Shu, J. An, W.B. Ding, X.Y. Liu, S.Y. Wang, C. Zhao, H. Y. Yu, H. Wang, C. Wang, X.P. Fu, X.X. Pan, G.M. Xie, Z.L. Wang, Underwater wireless communication via TENG-generated Maxwell's displacement current, Nat. Commun. 13 (2022), https://doi.org/10.1038/s41467-022-31042-8.
[27] T. Zhao, M. Xu, X. Xiao, Y. Ma, Z. Li, Z.L. Wang, Recent progress in blue energy harvesting for powering distributed sensors in ocean, Nano Energy 88 (2021), https://doi.org/10.1016/j.nanoen.2021.106199.
[28] M. Xu, P. Wang, Y.-C. Wang, S.L. Zhang, A.C. Wang, C. Zhang, Z. Wang, X. Pan, Z. L. Wang, A. Soft, and Robust spring based triboelectric nanogenerator for harvesting arbitrary directional vibration energy and self-powered vibration sensing, Adv. Energy Mater. 8 (2018), https://doi.org/10.1002/aenm.201702432.
[29] Y. Qi, G. Liu, Y. Gao, T. Bu, X. Zhang, C. Xu, Y. Lin, C. Zhang, Frequency band characteristics of a triboelectric nanogenerator and ultra-wide-band vibrational energy harvesting, ACS Appl. Mater. Interfaces 13 (2021) 26084–26092, https://doi.org/10.1021/acsami.1c06031.
[30] H. Zhao, M. Shu, Z. Ai, Z. Lou, K.W. Sou, C. Lu, Y. Jin, Z. Wang, J. Wang, C. Wu, Y. Cao, X. Xu, W. Ding, A highly sensitive triboelectric vibration sensor for machinery condition monitoring, Adv. Energy Mater. 12 (2022), https://doi.org/10.1002/aenm.202201132.
[31] G. Xu, C. Li, C. Chen, J. Fu, T. Hou, Y. Zi, Dynamics of triboelectric nanogenerators: a review, Int. J. Mech. Syst. Dyn. (2022), https://doi.org/10.1002/msd2.12058.
[32] P. Vasandani, Z.-H. Mao, W. Jia, M. Sun, Relationship between triboelectric charge and contact force for two triboelectric layers, J. Electrost. 90 (2017) 147–152, https://doi.org/10.1016/j.elstat.2017.11.001.
[33] S. Niu, S. Wang, L. Lin, Y. Liu, Y.S. Zhou, Y. Hu, Z.L. Wang, Theoretical study of contact-mode triboelectric nanogenerators as an effective power source, Energy Environ. Sci. 6 (2013), https://doi.org/10.1039/c3ee42571a.
[34] D. Kim, Y. Oh, B.W. Hwang, S.B. Jeon, S.J. Park, Y.K. Choi, Triboelectric nanogenerator based on the internal motion of powder with a package structure design, ACS Nano 10 (2016) 1017–1024, https://doi.org/10.1021/acsnano.5b06329.
[35] X. Xiao, X. Zhang, S. Wang, H. Ouyang, P. Chen, L. Song, H. Yuan, Y. Ji, P. Wang, Z. Li, M. Xu, Z.L. Wang, Honeycomb structure inspired triboelectric nanogenerator for highly effective vibration energy harvesting and self-powered engine condition monitoring, Adv. Energy Mater. 9 (2019), https://doi.org/10.1002/aenm.201902460.
[36] J. Chang, C. Zhu, Z. Wang, Y. Wang, C. Li, Q. Hu, R. Xu, T. Du, M. Xu, L. Feng, A full-set and self-powered ammonia leakage monitor system based on CNTs-PPy and triboelectric nanogenerator for zero-carbon vessels, Nano Energy 98 (2022), https://doi.org/10.1016/j.nanoen.2022.107271.
[37] X. Wang, S. Niu, F. Yi, Y. Yin, C. Hao, K. Dai, Y. Zhang, Z. You, Z.L. Wang, Harvesting ambient vibration energy over a wide frequency range for self-powered electronics, ACS Nano 11 (2017) 1728–1735, https://doi.org/10.1021/acsnano.6b07633.
[38] X. Zhang, J. Zhao, X. Fu, Y. Lin, Y. Qi, H. Zhou, C. Zhang, Broadband vibration energy powered autonomous wireless frequency monitoring system based on triboelectric nanogenerators, Nano Energy 98 (2022), https://doi.org/10.1016/j.nanoen.2022.107209.
[39] S. Hu, Z. Yuan, R. Li, Z. Cao, H. Zhou, Z. Wu, Z.L. Wang, Vibration-driven triboelectric nanogenerator for vibration attenuation and condition monitoring for transmission lines, Nano Lett. 22 (2022) 5584–5591, https://doi.org/10.1021/acs.nanolett.2c01912.
[40] Z.L. Wang, On Maxwell's displacement current for energy and sensors: the origin of nanogenerators, Mater. Today 20 (2017) 74–82, https://doi.org/10.1016/j.mattod.2016.12.001.
[41] S.M.S. Rana, M.T. Rahman, M. Salauddin, S. Sharma, P. Maharjan, T. Bhatta, H. Cho, C. Park, J.Y. Park, Electrospun PVDF-TrFE/MXene nanofiber mat-based triboelectric nanogenerator for smart home appliances, ACS Appl. Mater. Interfaces 13 (2021) 4955–4967, https://doi.org/10.1021/acsami.0c17512.

Hongyong Yu is currently pursuing his doctor degree in Dalian Maritime University, china. His current research interests in the triboelectric nanogenerators and vibration energy harvesting.

Ziyue Xi is currently pursuing his master degree in Dalian Maritime University, China. His current research interests include vibration energy, self-powered systems and triboelectric nanogenerators.

Yiping Zhang is currently pursuing his master degree in Dalian Maritime University, China. His current research interests include acoustic energy, self- powered systems and triboelectric nanogenerators.

Ruijiang Xu is currently pursuing his master degree in Dalian Maritime University. His current research interests include triboelectric-nanogenerators and blue energy.

Cong Zhao is currently pursuing his doctor degree in Dalian Maritime University, China. His current research interests include self-powered system, intelligent marine equipment monitoring and triboelectric nanogenerator.

Yawei Wang is currently pursuing his master degree in Dalian Maritime University, China. His current research interests include triboelectric-nanogenerators and blue energy.

Xinyang Guo is currently pursuing his master degree in Dalian Maritime University, China. His current research interests in high voltage TENG and self-powered systems.

Yue Huang is currently studying for a master's degree at Dalian Maritime University, China. Her current research interests are triboelectric nanogenerators and environmental micro energy.

Prof. Jianchun Mi received his Ph.D. degrees from Newcastle University in 1995. He was a national researcher and director researcher of Adelaide University in Australia from 1995 to 2006. He joined Peking University in 2006, and now he is a full professor in the College of Engineering. His research interests include turbulence, combustion and renewable energy.

Yejin Lin received his Ph.D. degree from Dalian Maritime University in 2007. Now he is a Professor in Marine Engineering College, Dalian Maritime University. His current research is mainly focused on the areas of marine engineering automation, artificial intelligent control and sensor technology.

Taili Du received his B.S. and M. S. from Dalian Maritime University in China in 2008 and 2010. Since 2010, he is with Dalian Maritime University where he is currently an Associate Professor. Currently, he is as a doctoral candidate in Marine Engineering College, Dalian Maritime University. His current research work focus on intelligent equipment performance monitoring and self-powered sensor based on Triboelectric Nanogenerator.

Minyi Xu received his Ph.D. degree from Peking University in 2012. During 2016–2017, he joined Professor Zhong Lin Wang' group at Georgia Institute of Technology. Now he is a Professor in the Marine Engineering College, Dalian Maritime University. His current research is mainly focused on the areas of blue energy, self-powered systems, triboelectric nanogenerators and its practical applications in smart ship and ocean.